

# We are IntechOpen, the world's leading publisher of Open Access books Built by scientists, for scientists

6,900

Open access books available

185,000

International authors and editors

200M

Downloads

Our authors are among the

154

Countries delivered to

TOP 1%

most cited scientists

12.2%

Contributors from top 500 universities



WEB OF SCIENCE™

Selection of our books indexed in the Book Citation Index  
in Web of Science™ Core Collection (BKCI)

Interested in publishing with us?  
Contact [book.department@intechopen.com](mailto:book.department@intechopen.com)

Numbers displayed above are based on latest data collected.  
For more information visit [www.intechopen.com](http://www.intechopen.com)



# A Heat Flux Microsensor for Direct Measurements in Plasma Surface Interactions

Dussart Rémi, Thomann Anne-Lise and Semmar Nadjib  
GREMI, University of Orleans/CNRS  
France

## 1. Introduction

The energy transfer from a plasma to a surface always plays an important role in low pressure plasma material processing (deposition, etching, surface treatment...) [1, 2]. Three different types of plasma species interact with the surface: charge carriers, neutrals and photons [3]. The energy due to charged particles (mainly ions and electrons) represents a significant contribution, especially when the substrate is biased. The energy coming from neutrals can be divided into different contributions: gas conduction, metastable de-excitation, fast neutrals (sputtered atoms, charge transfer mechanisms,...) and reactions at the surface (e.g. chemical etching...). In argon, for example, the energy due to neutrals is shared between gas conduction and metastable de-excitation since no reaction occurs at the surface. In reactive plasmas, the energy contribution of chemical reactions between radicals and substrate materials can be very high and has to be considered as well.

From the results of conventional plasma diagnostics (knowledge of flux and energy carried by interacting species), it is possible to estimate the maximum energy that can be transferred to a surface through energy balances. But the true energy delivered during plasma/surface interaction is difficult to evaluate. Thus, it might be more accurate to perform direct measurements of the energy influx. Most of the techniques used until now only lead to indirect estimations (eg. time evolution of the substrate temperature) [3]. These methods only give a posteriori values averaged over several minutes, although for most processes (especially time resolved ones) real time measurement of the energy flux would be of interest.

To make direct heat flux measurements in plasma processes, we proposed to use a commercially available heat flux microsensor (HFM) [4]. This HFM is composed of hundreds of integrated micro thermocouples, which form a thin thermopile having a very good time resolution (<10 ms). In the following section, we present in details the diagnostic and the experimental setup we used to make measurements. Then, we will explain the method we used to calibrate it. The third section will describe the different contributions in the total energy transfer from a plasma to a surface. In the fourth section, measurements of the energy transfer from an inductively coupled plasma of argon to the HFM will be presented. Special diagnostics such as Langmuir probe and diode laser absorption have been used to evaluate the contribution of the different species (eg. charged particles, neutrals, metastables,...) in the total measured energy flux. In section five, we show an example of the evaluation of the energy flux due to chemical reactions between fluorine

radicals produced by an  $\text{SF}_6$  plasma and a substrate of silicon. In the last section, some measurements of the energy flux in a plasma sputtering deposition experiment are presented and show the good sensitivity of the diagnostic.

## 2. Detailed description of the diagnostic

### 2.1 Heat flux sensor

The Heat Flux Microsensor is produced by Vatel Corporation based in Virginia in the United States [5]. The sensor mounted on the rod is shown in figure 1(a). The active surface, which is shown in the inset of figure 1(a), has a 6 mm diameter. It is composed of two distinguished sensors. The first one is a thermopile made in Nichrome and Constantan [5] based on Seebeck effect. A simple drawing is shown in figure 1(c) to explain this effect. Thermocouples are mounted in series. The junctions are located on two different levels of the sensor (figure 1(b)). Each thermocouple produces a voltage which is proportional to the heat flux, which is transferred from the top surface to the bottom of the sensor. The HFM proposed by Vatel is composed of hundreds of thermocouples ( $1600 \text{ cm}^2$ ) fabricated by thin film deposition processes. When submitted to an energy influx, a very low temperature gradient appears between both levels of thermocouples which results in a very low voltage for each thermocouple. But, since there is a quite high density of these thermocouples, the resulting voltage is high enough to be measured by a nanovoltmeter. The second sensor is a Pt100 temperature sensor surrounding the thermopile. The PT100 is used to control the sensor temperature. Note that this second sensor is not necessary in our experiment to measure the energy flux. Moreover, by making this temperature measurement, some heat is produced which can perturb the heat flux evaluation.

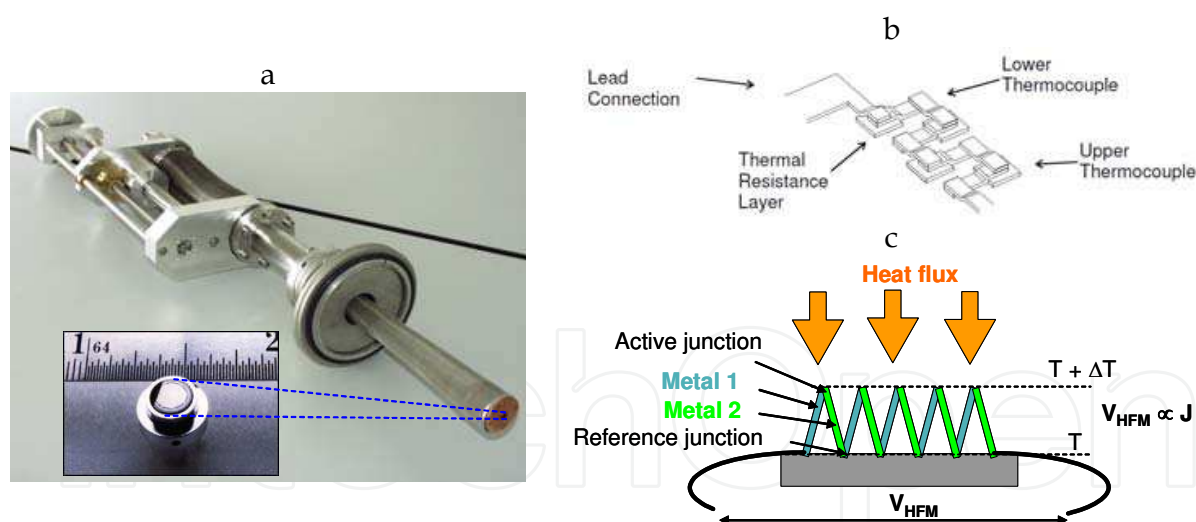


Fig. 1. (a) Heat flux microsensor mounted on the translating rod (inset) Picture of the active surface, (b) Schematic of the thermopile at the microscopic scale, (c) drawing showing the seebeck effect principle

Both sensors are inserted in a copper chamber cooled by water and controlled in temperature. For our experiments, we used the HFM-7 model, which can hold a temperature as high as  $700^\circ\text{C}$ . The intrinsic response of the thermopile sensor is  $17 \mu\text{s}$ . However, the sensor is coated with a black paint in order to ensure radiation absorption. The presence of this coating increases the time response up to  $300 \mu\text{s}$ .

Before placing the HFM inside a low pressure plasma, a calibration of the sensor has to be carried out, which is described in the next section.

2.2 Calibration procedure

For the calibration procedure, the whole sensor is placed in front of a cylinder black body (BB) (Figure 2). The temperature of the HFM ( $T_1$ ) is fixed by the controller and the BB temperature ( $T_2$ ) is varied from ambient to 250 °C. A thermo-radiative energy transfer takes place between the BB and the HFM, that can be calculated using the Stefan law [6]. The temperature of the back side heat flux sensor is maintained to 5°C and does not deviate during the calibration. This was done to avoid the increase in the sensor temperature, which would lead to radiation loss by IR emission.

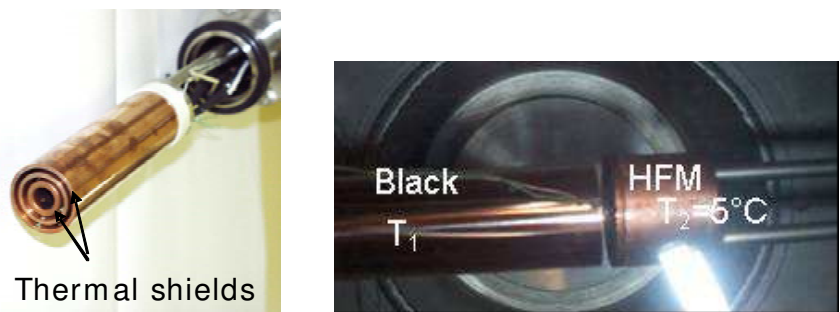


Fig. 2. Picture of the black body (left) and top view of the calibration experiment (right)

According to the NIST Protocole we used, the calibration is first conducted in the equilibrium regime: the radiative transfer exchange is considered only when the BB averaged temperature and output signal of the HFM lead to stabilized values. Then, using the radiative heat exchange balance, the correlation between the radiative heat flux density and the output electrical signal provided by the HFM can be made. We have also conducted a calibration procedure under a dynamic regime, which gives similar results as in the equilibrium regime (Figure 3). When we investigated the calibration procedure, we showed that gas convection took place even at relatively low pressure, which prevent's from the knowledge of the transferred energy [4]. Thus, calibration of the sensor must be carried out in vacuum ( $10^{-5}$  Pa).

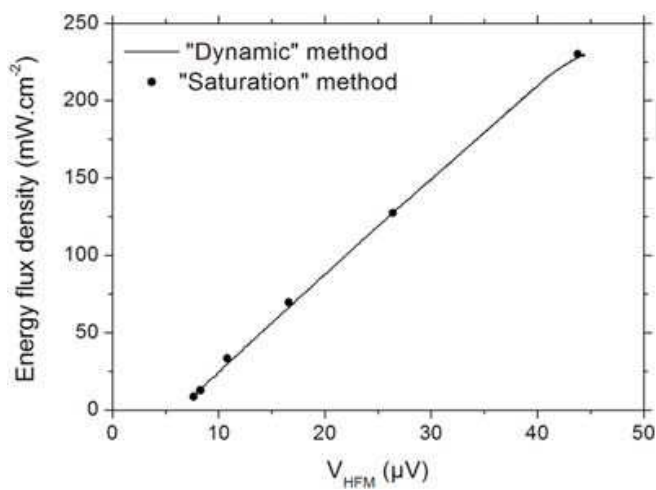


Fig. 3. Calibration curve under vacuum: comparison between dynamic measurements (line) and values taken at saturation (circles).

2.2.1 Calibration with thin samples

It is known that the energy transferred during interaction of particles with a surface widely depends on the surface characteristics (chemical composition, morphology etc.). It is thus of particular relevance to perform heat flux measurements on true samples.

The calibration curve plotted in figure 3 was recorded on the bare HFM surface. When a sample is placed in front of the HFM, assumption has to be made on its surface temperature in order to find the relationship between the HFM signal and the corresponding radiative heat flux at the sample surface. In a first approach to determine the real surface temperature, a 1D conduction model of a radiatively heated thin solid is computed using SCILAB®. We demonstrate that the temperature difference between front and back faces of 0.5mm thin solids does not exceed  $5.10^{-3}$  K for both, Si and Cu samples. Secondly a 3D conduction simulation of the process is performed with COMSOL multiphysics to compute temperature and heat flux fields over the whole sample. The main studied parameter is the thermal contact resistance ( $R_{ctc}$ ) appearing between the sample and the HFM [7]. Two important points are particularly detailed: the time for samples to be at thermal steady state and the heat flux values.

As explained above before the calibration procedure consists in heating the black body at different temperatures with different voltages and evaluating the radiative heat flux density using the Stefan law [6]

$$\varphi_{BB/HFM} = \sigma \cdot (a_{HFM} \cdot \varepsilon_{BB} \cdot T_{BB}^4 - a_{BB} \cdot \varepsilon_{HFM} \cdot T_{HFM}^4)$$

(1)

$T$ ,  $a$ ,  $\varepsilon$  are respectively the absolute temperature, absorptivity and emissivity of the black body (BB) and the HFM microsensor (HFM).  $\sigma$  is the stefan-boltzmann coefficient and  $\phi$  the flux density of the radiative heat transfer.

The corresponding HFM voltage is displayed on the nanovoltmeter while the BB temperature increases. In case of bare HFM sensor, absorption and emission coefficients are assumed to be unity since the active surface is black painted [8]. However absorptivity and emissivity must be adjusted when a sample is fixed against the HFM probe. The view factor is set equal to 1 because of the short distance between the blackbody and the fluxmeter and because their active areas are similar. The net radiative heat flux density exchanged between a blackbody and a grey surface is deduced from the following expression [6]

$$\varphi_{BB/sample} = \sigma \cdot \varepsilon_S \cdot (T_{BB}^4 - T_S^4)$$

(2)

S label stands for sample surface

Samples are thin solids of copper and (001)-silicon of 15×15 mm<sup>2</sup> surface and 0.5 mm thickness (e). The former is frosted in order to remove the major part of the oxide layer whereas silicon has no particular treatment. The thermo-physical properties used in our calculations are summarized in table 1:

	Density $\rho$ (kg.m <sup>-3</sup> )	Surface emissivity $\varepsilon_s$	Thermal conductivity $\lambda$ (W.m <sup>-1</sup> .K <sup>-1</sup> )	Heat capacity $C_v$ (J.Kg <sup>-1</sup> .K <sup>-1</sup> )
Copper	8960	0.1	385	385
Silicon	2330	0.65	120	740

Table 1. Thermo-physical properties of Cu and Si at low temperatures



Thermal properties of samples are extracted from values provided in literature [7]. Taking into account their temperature dependence, these values were extrapolated for room temperature of sample surfaces.

HFM voltage is plotted versus time in figure 4. The blackbody temperatures given in the legends correspond to the thermal equilibrium with the HFM or the sample if it is present. On this figure, it is clearly seen that the HFM voltage at saturation, i.e. the heat flux density, is different depending on both the BB temperature and the sample nature. Furthermore, for a given BB temperature, the HFM voltage is related to the presence of a sample in front of its surface. This behaviour, that seems irrational at first glance, can be explained by the difference in collecting areas with or without sample. As a matter of fact, the microsensor active area is only 28.3 mm<sup>2</sup> whereas the collecting one in presence of a sample is 225 mm<sup>2</sup>. The difference between Si and Cu curves is mainly due to the emissivity ratio and is in agreement with the expected values.

The offsets, different from zero, indicates that heat flux is collected even at ambient temperature. This is explained by the radiative flux between the vessel at room temperature and the HFM at lower temperature (298K).

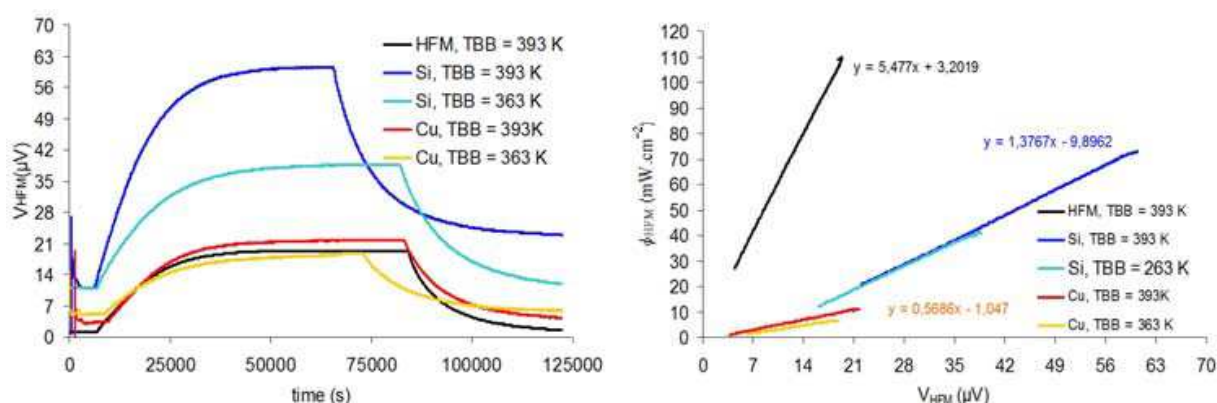


Fig. 4. Experimental measurements of heat flux density ( $V_{HFM}$ ) on the left and dynamic calibration curves on the right side with respect to the black body temperatures ( $T_{BB}$ ) at low pressures ( $\sim 10^{-5}$  Pa)

As explained above and according to the NIST calibration protocol, the calibration curves are also plotted on the right graph of figure 4. Thanks to the calibration line equations deduced from this graph, one can measure the heat flux density arriving on the HFM surface or on thin solid samples, whatever the nature of the heat source (collisions, radiation...). However these results have to be used with care since rough assumptions on the sample emissivity have been made (theoretical values). Moreover the sample surface temperature has been supposed to be the same as the cooled HFM, which might be not true in the present configuration of the system. In order to get more accurate results, sample surface temperature is estimated from the resolution of a 1-D heat balance.

### 2.2.2 1D Modelling of thin sample on HFM

At stationary state, the heat flux crossing a thin solid sample could roughly be supposed in equilibrium with the heat exchanged at the surface of the solid. Furthermore, no heat loss is considered through the lateral faces of the sample, which is surrounded by an insulator.

$$\phi = \frac{\lambda}{e} \cdot (T_S - T_b) \cdot S_m = \varepsilon \cdot \sigma \cdot (T_{BB}^4 - T_S^4) \cdot S_{BB} \tag{3}$$

where  $S_{BB}$  stands for the surface radiated by the black body,  $T_b$  the temperature at the backside of the sample and  $S_m$  is an averaged surface smaller than  $S_{BB}$  but greater than the active area of the heat probe as shown in figure 5.

We have then to resolve a 4-order polynomial

$$P_4(T_S) = \varepsilon \cdot \sigma \cdot S_{BB} \cdot T_S^4 + \frac{\lambda}{e} \cdot S_m \cdot T_S - \left( \varepsilon \cdot \sigma \cdot S_{BB} \cdot T_{BB}^4 + \frac{\lambda}{e} \cdot S_m \cdot T_b \right) = 0 \tag{4}$$

with  $T_{BB} = f(t)$  and  $T_b = T_{HFM} = 278.15K$

The curves reported hereafter are results obtained when solving relation (4) with SCILAB code. The BB and HFM temperatures are the time dependent input data derived from experiments whereas the surface temperature of the sample is the unknown parameter. Note that its value is determined at saturation. The results presented in figure 5a demonstrate that the temperature( $T_S$ ) difference between the front and the back ( $T_{HFM}$ ) side of the thin solid is of the order of  $10^{-3}K$  for silicon and around  $10^{-4}K$  for Cu samples. These values are so insignificant that the approximation made in previous chapter, stating  $T_S = T_{HFM}$ , is justified.

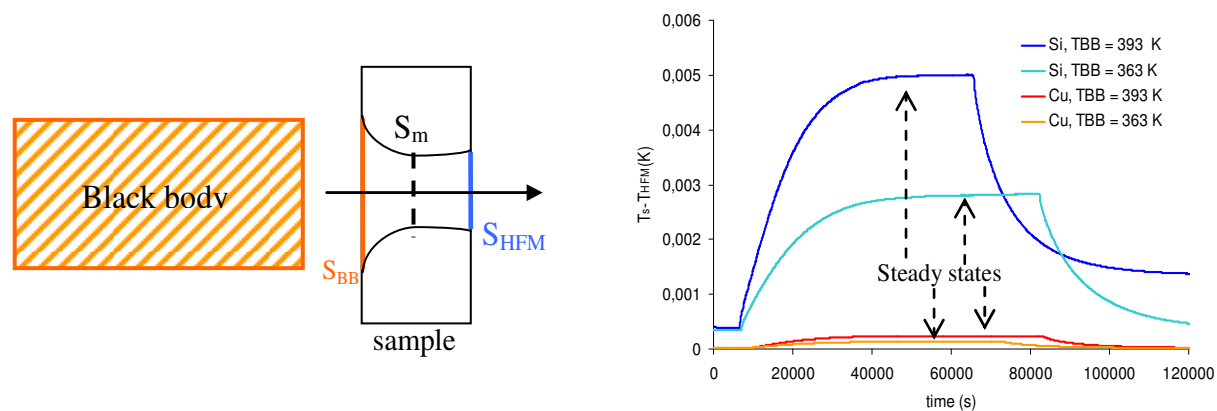


Fig. 5.a Scheme used for the 1D model (left) and temperature difference for Cu and Si obtained from 1-D model simulation (right).

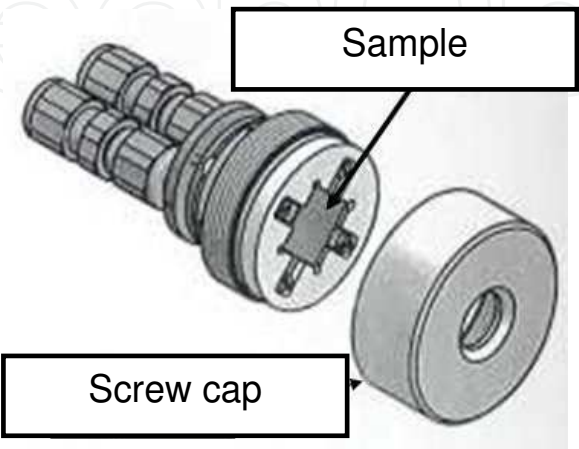


Fig. 5.b Schematic view of the sample fixation of the HFM using a screw element

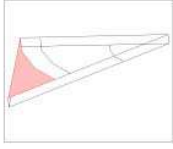
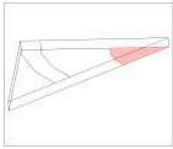
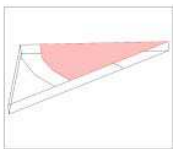
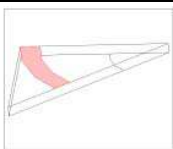
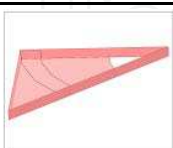
However, it is important to notice that the model does not consider the existence of a thermal contact resistance between the HFM surface and the sample, since  $T_b$  has been taken equal to  $T_{HFM}$ . Unfortunately, this contact may not be perfect. Thus, a 3-dimensionnal study of the problem is necessary to have the best approach of our system.

2.2.3 Full 3D modelling of thin sample on HFM

Our thermal system is simulated with COMSOL multiphysics. In fact, only the sample is built, whereas the heat fluxes and temperatures are given as boundary conditions. Since the thermal contact resistance is not directly accessible in the code, it is simulated as a particular convective boundary condition at the HFM/substrate interface, where the convective heat coefficient and the thermal contact resistance are related by the following equation:

$$h = \frac{1}{R_{ctc}}$$

(5)

Boundaries	Heat flux density	Parameters
	Rarefied gas only $\varphi = h.((T + 2) - T)$	$h = 3.\beta.\sqrt{\frac{k_B.P_{gas}}{2.\pi.m_{gas}.T}} W.m^{-2}.K^{-1} *$
	Cooling bath $\varphi = \frac{1}{R_{ctc}}.(T_{HFM} - T)$	$T_{HFM} = 278.15 K ;$ $R_{ctc} = 10^0, 10^{-1} ... 10^{-7} m^2.K.W^{-1}$
	Black body radiated area $\varphi = h.((T + 3) - T) + \varepsilon.\sigma.(T_{BB}^4 - T^4)$	$T_{BB} = 373.15 K$
	Screw cap presence $\varphi = \frac{\lambda_{cap}}{e_{cap}}.((T + 2) - T)$	$\lambda_{cap} = 0.25 W.m^{-1}.K^{-1} ; e_{cap} = 3.10^{-3} mm$
	Insulated areas $\varphi = 0$	Either external boundaries or symmetry axis

\* formula extracted from [9]

Table 2. Thermo-physical parameters used in this work

In the vicinity of the surface sample, the temperature of the rarefied gas is close to the solid one. To estimate the maximum heat loss from the surface,the gas temperature is here voluntarily increased by 2K or 3K, depending on how far the heat source (BB) is located. For the same reason, the screw cap temperature is also set at 2K over the solid surface one (fig. 5-b).



Owing to the plans of symmetry existing in the squared sample, the geometry of the problem has been reduced at one eighth for the sake of finer meshing and fast computer calculations. The whole boundaries conditions are summarized in table 2.

As shown in figure 6, the low temperature difference between the front and the back side of the thin sample ( $\Delta T_{\text{sample}}$ ), already obtained from 1D model is confirmed in a full 3D modelling, whatever the thermal contact resistance value. Moreover, the temperature difference in silicon sample is found approximately ten times higher than in copper , again in good agreement with the 1D model..

One can also see on figure 6 the effect of  $R_{\text{ctc}}$  on the delay to reach the steady state. As expected, the lower is the thermal contact resistance; the faster the equilibrium regime is reached. Note that the time expressed here could not be compared with the experiment one, which strongly depends on the blackbody inertia. In simulations, the blackbody temperature being immediately set at 373 K, the time evolution is only characteristic of the thermal response of the system (cooled HFM with sample)

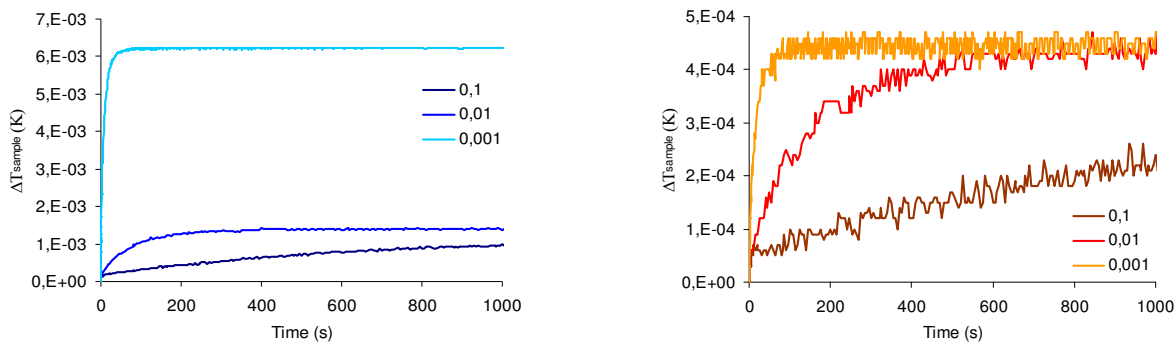


Fig. 6. Difference of front and back temperatures for Si (left) and Cu (right), at various thermal contact resistances (in  $\text{m}^2.\text{K}.\text{W}^{-1}$ ) obtained from full 3D- model

The front ( $T_s$ ) and the back ( $T_b$ ) side temperatures of the sample presented in figure 7 are strongly dependent on the thermal contact resistance. It is seen that the temperature of the surface sample may be different from that of the cooling bath i.e. 278 K, even for weak thermal contact resistances.

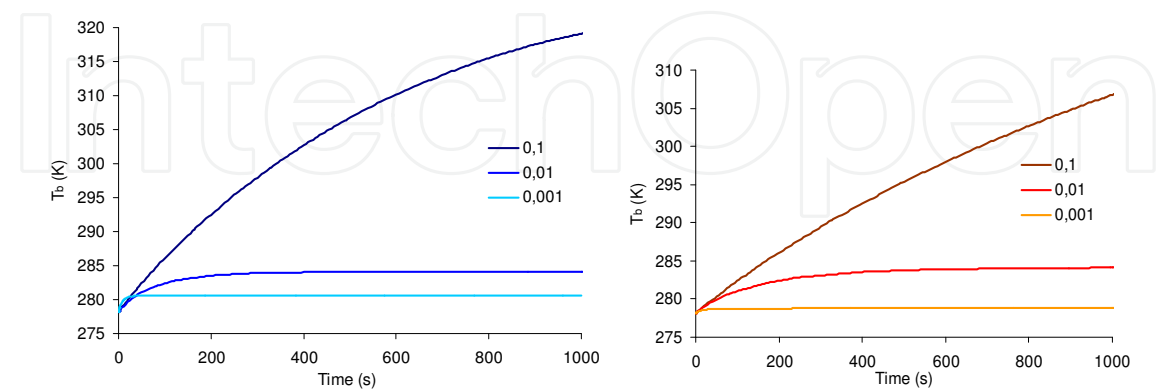


Fig. 7. Simulation of the temperature time evolution at the back face of the sample for Si (left) and Cu (right) for several thermal contact resistances, from full 3D- modelling

Simulated heat flux reaching the fluxmeter is plotted in figure 8. In the full 3D-computations, the heat fluxes are calculated for a black body radiating at 373 K. One could

easily notice that measured heat fluxes are close to the calculated ones. This result indicates that thermal contact resistance values are in the range  $10^{-3}$  to  $10^{-1}$   $\text{m}^2.\text{K}.\text{W}^{-1}$ , which is in good agreement with values given in literature for solid-solid thermal contact resistances [6].

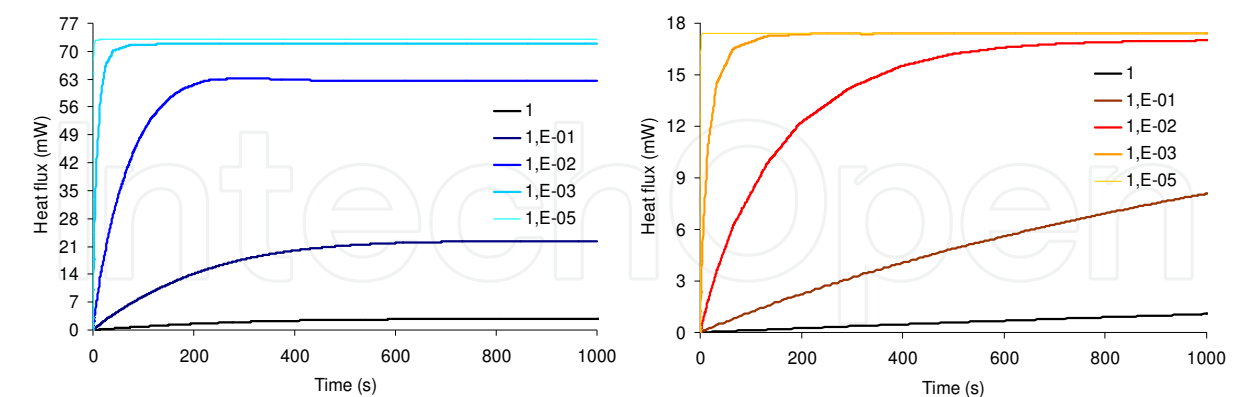


Fig. 8. Simulation of heat flux time evolution at the HFM surface for Si (left) and Cu (right) samples, at various thermal contact resistances (in  $\text{m}^2.\text{K}.\text{W}^{-1}$ ), from full 3D- modelling

It is interesting to compare heat fluxes deduced from experimental curves with those calculated by 3D-simulations in similar conditions. This is summarized in table 3.

Samples	T <sub>BB</sub> (°C)	Experiments	3D simulations for T <sub>BB</sub> = 373K			
			R <sub>ctc</sub> (m <sup>2</sup> .K.W <sup>-1</sup> ) =	10 <sup>-1</sup>	10 <sup>-2</sup>	10 <sup>-5</sup>
Copper	363K	12.5 mW		13 mW	17 mW	17.5 mW
	393K	16 mW				
Silicon	363K	53 mW		21 mW	63 mW	74 mW
	393K	92 mW				

Table 3. Comparisons of measured and 3D simulated heat fluxes (values given for saturation states) for Cu and Si samples

2.3 Comparison with other heat flux probes

Since the 1960s many authors tested various techniques to measure the energy influx [10-12]. Results provided by the literature most often come from calculations based on temperature measurements [13, 14]. Among them, calorimetric probes, based on an original idea of Thornton [10], were successfully applied to plasma science [15-18]. Some sophisticated thermal probes have been developed [19-21], such as for example the one designed in the IEAP Kiel, which consists of a thermocouple brazed to a metal plate (substrate dummy). This probe has been used by Kersten et al to characterize many kinds of low pressure plasmas used for powder generation, space propulsion, PECVD, etc [17, 21]. Nevertheless, with this kind of probes, the total energy flux is always estimated a posteriori from thermograms recorded during the heating and cooling steps. Mathematical treatments are then employed to estimate the heat flux, which introduce systematic deviations. Moreover, with these kinds of probes, it is not possible to evidence transfer mechanisms of different kinetics such as transfer by collision (instantaneous) or transfer involving a heating step (IR emission). Detection of transient or small energetic contributions (several  $\text{mWcm}^{-2}$ ) could not be reasonably achieved.

To illustrate results that can be obtained by calorimetric probes and by the HFM, typical signals recorded in an RF argon discharge are presented in Fig. 9. Even if HFM measurements last about 100s, it is seen on the graph that a stabilized voltage is reached within several seconds. The corresponding energy influx value is directly deduced from the calibration curve. In the case of the calorimetric probe, the thermogram has to be recorded at least during 120s in order to be further treated by a software to calculate the influx. The offset value (close to  $2.5\text{ }\mu\text{V}$ ) observed on the HFM graph between two signals is due to radiative transfer between the chamber and the sensor kept at 298K. To determine the energy influx only due to the RF plasma, the voltage difference between the offset and the plasma-on signal has been taken into consideration.

Due to the sensitivity of the thermopile (thin film design) the noise on the HFM voltage signal is very low, even at low energy flux density values. Consequently, the corresponding energy influxes are determined with minor errors. In comparison, the signals obtained by the calorimetric probe for RF power less than 60W (e.g. energy influxes less than  $35\text{mWcm}^{-2}$ ) are rather noisy. This fact induces an additional source of error. The increase of the background temperature in this case may also lead to errors on the determination of the influx.

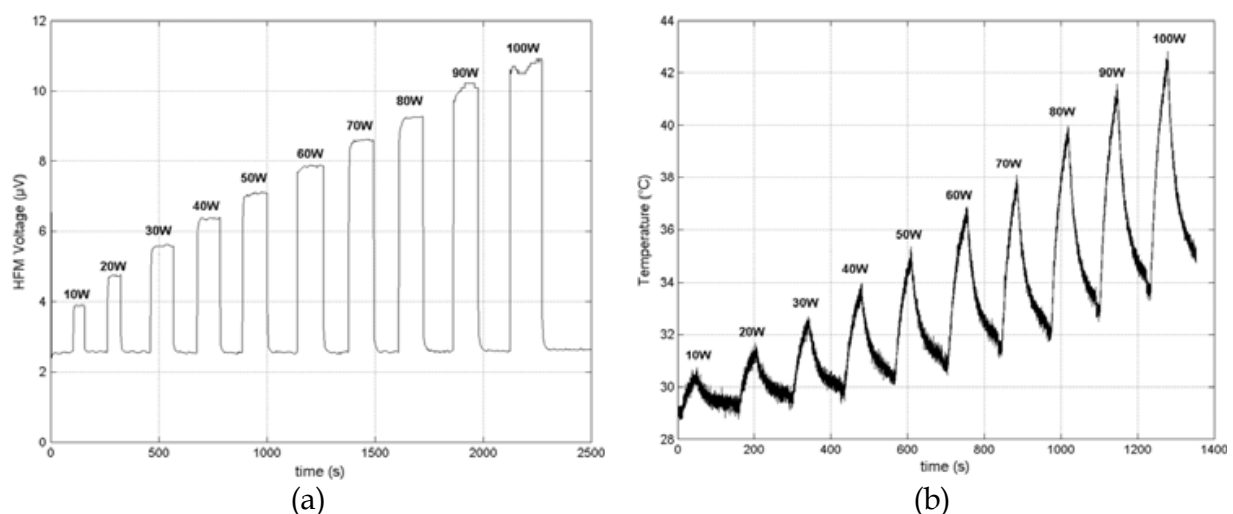


Fig. 9. (a) Temporal evolution of the HFM voltage in a asymmetric RF discharge for different input powers, (b) temporal evolution of the temperature for the calorimetric probe in an asymmetric RF discharge for different input powers

Comparison that we have done in previous work has evidenced drawbacks and advantages of both sensors [22]. The main advantage of the calorimetric probe is its low cost, simplicity and sturdiness. It has been shown that this probe provides reliable results in high energy plasma processes as plasma jet, ion beam and magnetron discharge [3, 21, 23]. However, the energy influx evaluation method can cause errors of about 10%. The method also requires a certain acquisition time (seconds to minutes) which can be a problem for detecting low energy contributions or transient energy transfer processes. Thus, the calorimetric probe is a cheap and powerful tool for the measurements of total energy influxes when detection of fast transfer processes is not required.

The main HFM drawbacks are its high cost and fragility. High energy influxes can damage thermopile, but this problem has been solved by positioning a substrate (copper) foil in front of the sensor. The HFM is characterized by a very good time resolution which can even be increased by the ablation of the black coating (zynolithe) and the optimization of the

acquisition system. The HFM is an interesting tool to separate energetic contributions and detect low energy influxes. This will be illustrated in the examples given in the following sections.

### 3. Energy influxes involved in plasma surface interaction

The different contributions in the energy flux are detailed in a review article [3]. We explain the main contributions, which will be useful for the examples of measurements we present in the next sections.

The thermal power which is transferred at the surface of a material immersed in a plasma is the sum of the following energy fluxes:

- radiation flux  $J_{rad}$  (plasma and reactor wall radiation)
- energy flux due charged particles  $J_{ch}$  (electrons and ions)
- energy flux due to neutrals  $J_n$  (gas conduction, metastable destruction at the surface ( $J_{met}$ ), adsorbed species ( $J_{ads}$ ), chemical reactions ( $J_{react}$ ) and rapid neutrals).

The total power  $P_{in}$  is given by :

$$P_{in} = \int_A (J_{rad} + J_{ch} + J_n) dS \quad (6)$$

$A$  is the surface area of the sample interacting with the plasma.

#### 3.1 Radiation

Heating by radiation can be due to reactor walls, which emit an IR radiation.

A part of the radiation flux  $J_{rad}$  corresponds to direct radiation of the plasma by excited states of the different species.

The energy transfer contribution of the reactor walls is usually quite weak in classical reactors [3]. To evaluate the part due to plasma radiation, one can use the following expression [24] :

$$J_{rad,p} = \xi_{ph} j_{ph} E_{ph} \quad (7)$$

$\xi_{ph}$  is the absorption probability of the photon by the surface. It depends on the material.

According to [14],  $J_{rad}$  contribution remains of the order of 5 to 10 % of the total energy in a TCP discharge working at 100 W in Argon.

#### 3.2 Electrical charges

In most of cases, charged particles ( $J_{ch}$ ) represent the most significant contribution in the energy flux. [3]

For positive ions, the kinetic energy acquired in the sheath, the recombination energy lost at the surface and the secondary electron emission have to be considered to evaluate their contribution in the energy transfer. One part only of the ion kinetic energy is transferred to the surface. To estimate the energy of the ions at the surface, their energy distribution function (IEDF) has to be determined. However, the maximum energy flux density can be estimated. It corresponds to the energy flux density, which would be transferred if no energy loss by collisions occurred in the sheath and if the whole ion energy (kinetic energy and recombination energy) was transferred to the surface without reemitting any secondary electrons or sputtered atoms. In the case of a non collisional sheath, ( $\lambda_i > d_{sh}$  : the mean free path of ions is greater than the sheath thickness), the energy flux is perpendicular to the

sheath. The Bohm criterium can be applied to estimate the incident ion flux, which is equal to the electron flux. The mean energy reaching the surface is equal to  $2k_B T_e$ , ( $k_B$ : Boltzmann constant and  $T_e$ : Electron temperature) [24].

Hence, the maximal energy flux due to charged particles is given by [24, 14] :

$$J_{ion} = 0,6 n_i u_B (2k_B T_e + e(V_P - V_S) + E_{rec}) \quad (8)$$

$n_i$  : ion density

$u_B$  : Bohm velocity

$T_e$  : electron temperature

$V_P$  : plasma potential

$V_S$  : surface potential

$E_{rec}$  : recombination energy

### 3.3 Neutrals

Neutrals can contribute under different manners in the energy transfer from the plasma to the surface. First, they can transfer energy by thermal conduction.

At low pressure, the power density  $\phi_{cond}$  from the plasma to the surface can be evaluated if we know the gas temperature. The « free molecule regime » can be applied if the mean free path of atoms is at least ten times greater than the sample dimensions [9]. In this case, the energy transfer linearly depends on pressure. The following expression (9) can be used to estimate the power density due to neutral conduction [9]:

$$\phi_{cond} = \sqrt{\frac{2k_B}{\pi m_{Ar}}} \frac{aP}{\sqrt{T_g}} (T_g - T_w) \quad (9)$$

with  $k_B$  : Boltzmann constant;  $m_{Ar}$  : Argon mass (40 uma) ; a: accommodation coefficient ; P: pressure (Pa) ;  $T_g$ : gas temperature in K and  $T_w$ : surface temperature in K.

The accommodation coefficient “a” has to be determined for Argon atoms bombarding the surface. The accommodation coefficient represents the atom thermalisation degree with the surface. It is defined by the following expression (10) [9]:

$$a = \frac{E_i - E_r}{E_i - E_w} = \frac{T_i - T_r}{T_i - T_w} \quad (10)$$

$E_i$ ,  $E_r$  and  $E_w$  represent the energy of the incident, reflected and surface atoms respectively. « a » is equal to 1 if atoms completely thermalize with the surface after interaction. According to [14], the accommodation coefficient is equal to 0.86 for argon.

At higher pressure (eg. 10 Pa), the energy flux by conduction of neutrals can become more significant. In this case, formula (9) cannot be applied because the regime is no longer the free molecule regime, but rather in so called « temperature jump regime », which corresponds to an intermediate regime between the free molecule regime and the normal conduction [9].

Metastable neutrals can bring a significant energy when they deexcite at the surface. In fact, the energy of  $1s_5$  and  $1s_3$  argon metastable levels reaches about 11 eV, which is the order of magnitude of the kinetic energy of the ions impinging the surface when it is not biased.

The power density  $\phi^*$  due to metastables is given by the following expression (11) [5]:

$$\phi^* = \xi^* N_m \sqrt{\frac{8k_B T_g}{\pi m_{Ar}}} E_m \quad (11)$$



with  $\xi^*$  the deexcitation probability ;  $N_m$  the metastable density.  $E_m$  the metastable energy (11.74 eV for  $1s_3$  and 11.56 eV for  $1s_5$  in the case of argon metastables).

$\xi^*$  strongly depends on the surface itself. It can vary from  $10^{-5}$  (for ceramics or oxidized surfaces) to 0.1-1 (catalytic surfaces) [5]. In our estimation, we took a value equal to 1 to have the maximum value of the power density due to metastable recombination.

In deposition processes, physisorption and chemisorption can also bring a significant value in the total energy flux [3]. In some particular cases, sputtered neutrals can get significant energies (e.g. 30 eV [3]) and should be taken into account as it will be shown in section 6. Finally, at higher pressure, in collisional sheath regimes, charge transfer can occur and create rapid neutrals [3].

### 3.4 Surface reactions

Chemical reactions between radicals of the plasma and the surface can bring energy (exothermal reactions) or consume energy at the surface (endothermal reactions). For example, in the case of silicon etching in plasmas containing fluorine atoms, we obtain the following reaction:



It is a very exothermal reaction whose enthalpy is  $-1931 \text{ kJ.mol}^{-1}$  [24,25]. Determining the etch rate, one can easily estimate the energy flux due to chemical reactions  $J_{\text{reac}}$  which is given by :

$$J_{\text{reac}} = \frac{\rho_{\text{Si}} v_g H_r}{M_{\text{Si}}} \quad (13)$$

$\rho_{\text{Si}}$  is the volumic mass of silicium.

$v_g$  is the etch rate

$H_r$  : is the reaction enthalpy

$M_{\text{Si}}$  : is the molar mass of silicium

An example of this contribution is presented in section 5.

## 4. Energy flux measurements in an Ar inductively coupled plasma

The HFM was directly submitted to an inductively coupled plasma of Argon. In this experiment, no substrate was mounted on the sensor. The HFM was left floating. Data were recorded by a sensitive nanovoltmeter as a function of time. The amount of energy influx due to the different species of the plasma was indirectly evaluated using other diagnostics (Langmuir probe, diode laser absorption, ...) which give plasma parameters such as ion density, electron temperature, gas temperature ...

In figures 10(a) and 10(b), we show respectively the obtained metastable temperature and the  $1s_5$  Ar metastable density versus RF power. Measurements were carried out by diode laser absorption experiments. Due to the large lifetime of the metastables, we assume they thermalize with other neutrals. Below 150 W, in capacitive regime, the gas remains at ambient temperature. Then, in inductive mode ( $P > 100 \text{ W}$ ), the gas temperature increases from about 400 K up to 600 K versus RF power. The change of regime is also observed in the metastable density curve (figure 10(b)). In capacitive mode, the  $1s_5$  metastable density increases versus power and reaches  $7.10^9 \text{ cm}^{-3}$ . In inductive mode, the  $1s_5$  density reaches  $9.10^9 \text{ cm}^{-3}$  at 200 W, then, it decreases versus RF power while electron density rises.

Metastables are mainly destroyed by quenching with electrons especially in inductive mode where electron density significantly increases [4]. At 600 W, the 1s<sub>5</sub> metastable density is about 3.10<sup>9</sup> cm<sup>-3</sup>.

To summarize energy balances calculated from plasma diagnostic, we plotted in figure 11 three different curves:

- energy flux directly measured with the HFM
- calculated energy flux due to charged particles (indirect evaluation by Langmuir probe measurements)
- calculated energy flux due to charged particles, gas conduction and metastables (gas temperature and meatastable densities given in figure 10 and energy flux calculated using equations 9,10, 11).

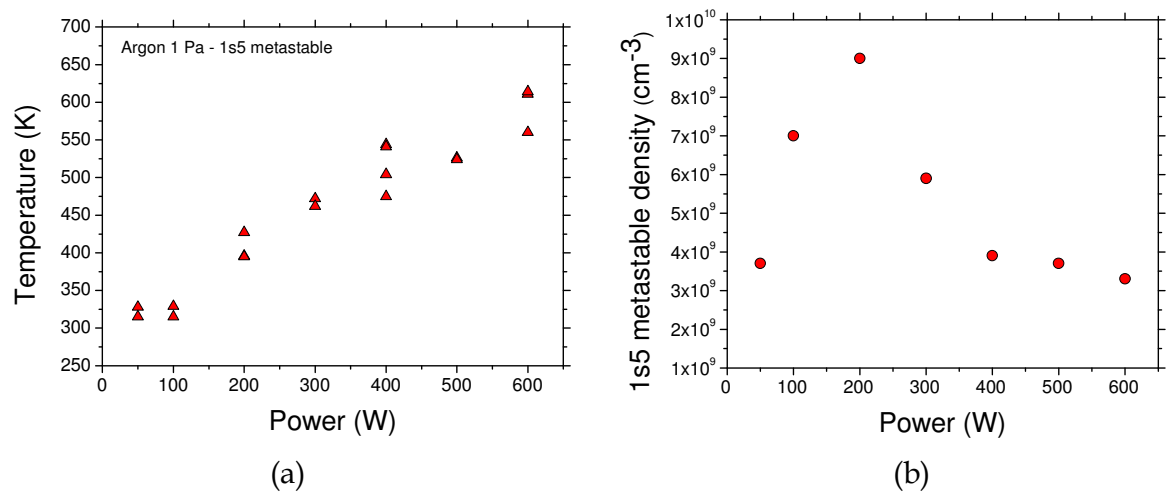


Fig. 10. (a) 1s<sub>5</sub> metastable temperature versus RF power,(b)1s<sub>5</sub> metastable density versus RF power

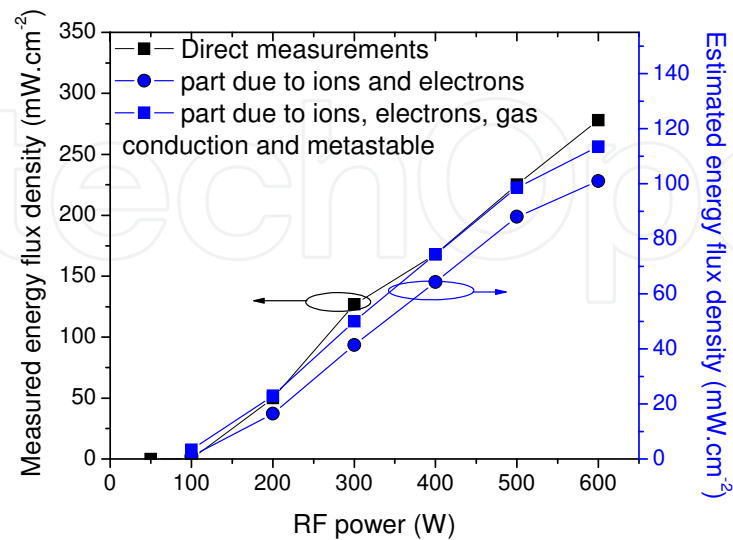


Fig. 11. Power density directly measured or estimated from energy balance versus RF power in an Ar Inductively coupled plasma

We concluded that, in our experimental conditions, most of the energy influx was due to ion bombardment. The contribution due to gas conduction corresponds to about 10 % of the total power density while the energy flux due to metastable de-excitation at the surface was found negligible. From Figure 11, it is seen that the measured heat flux density behaviour vs RF power is in good agreement with the estimations. The values are, nevertheless different, which is attributed to the fact that measurements by Langmuir probe are not very accurate. An error of the order of a factor of two can be typically made in such measurements.

### 5. Energy flux in a $\text{SF}_6$ plasma interacting with silicon

As seen in section 3, a silicon surface submitted to a  $\text{SF}_6$  plasma leads to very exothermal chemical reactions between fluorine radicals and silicon atoms at the surface. A measurement of the energy transfer due to these reactions was carried out by placing a silicon sample on the HFM and by submitting it to a  $\text{SF}_6$  inductively coupled plasma (figure 12) [26].

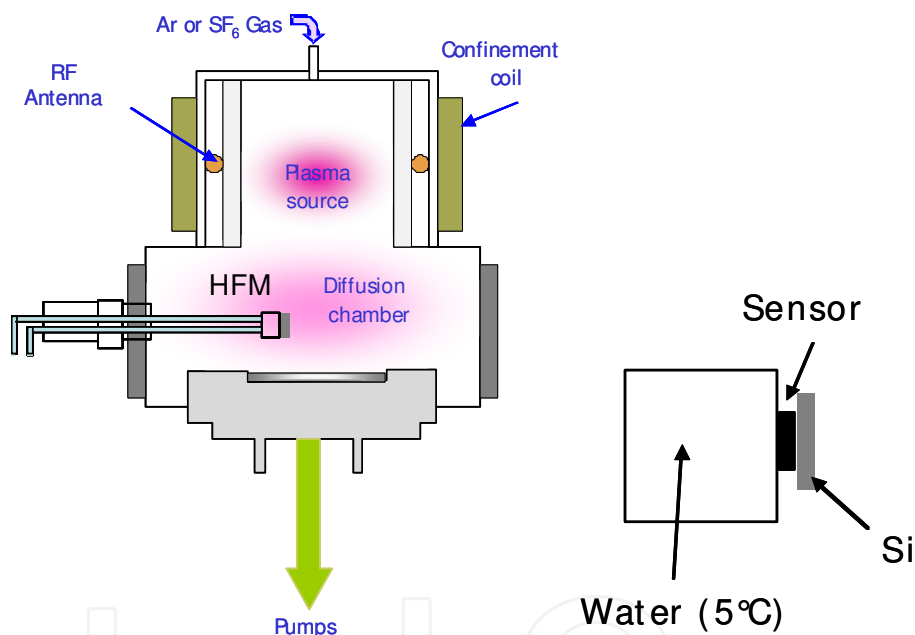


Fig. 12. (a) Schematic of the experiment to evaluate directly the energy flux due to chemical reactions, (b) detail of the sample mounted on the HFM

In figure 13(a), we show the results we have obtained by alternating Ar plasmas and  $\text{SF}_6$  plasmas when a silicon sample was mounted on the HFM. Whereas a low energy flux is measured in non-reactive atmosphere (in argon only physical interaction takes place), a high energy flux is obtained in  $\text{SF}_6$  plasma due to chemical reactions. The energy flux as a function of the plasma source power is presented in figure 13(b) in different cases. It is clear that low values are obtained in the case of Argon plasma or when the sample is oxidized, which decreases significantly the etch rate.

The energy flux due to chemical reactions is clearly demonstrated by these measurements. The reaction enthalpy was estimated by using the expression (13). We found a rather good agreement between our evaluation ( $-2200 \text{ kJ.mol}^{-1}$ ) and the theoretic value ( $-1931 \text{ kJ.mol}^{-1}$ ) [26].

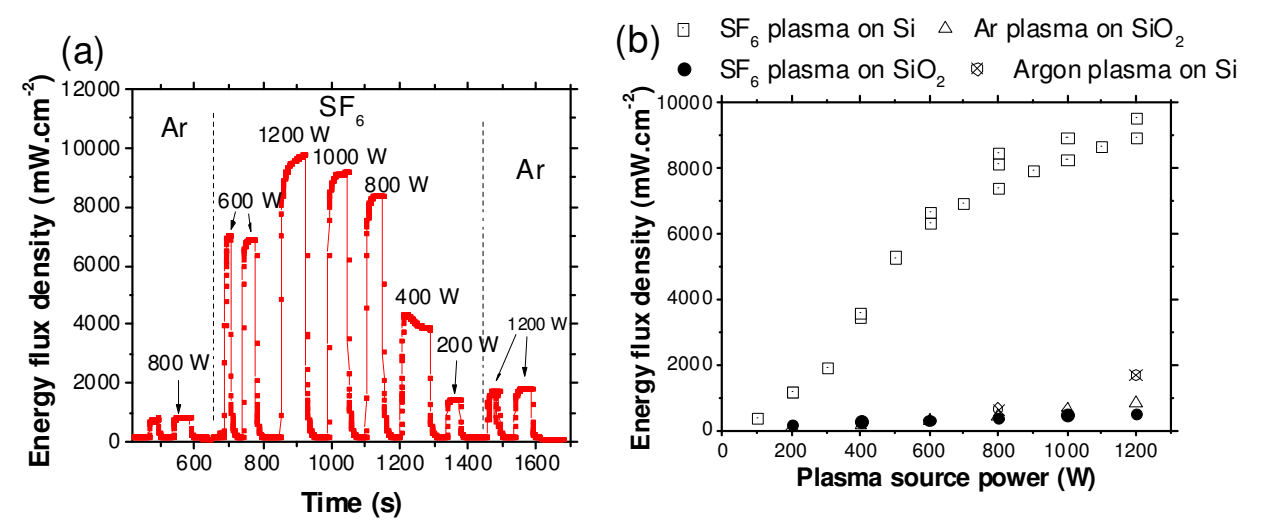


Fig. 13. (a) Time evolution of the HFM signal during an Ar plasma followed by a SF<sub>6</sub> plasma in interaction with a silicon sample for different source powers vs time. (b) Maximum energy flux density vs the source power density obtained for various plasma/substrate interactions (etching condition: SF<sub>6</sub>/Si; non-etching conditions: SF<sub>6</sub>/SiO<sub>2</sub>, Ar/SiO<sub>2</sub> and Ar/Si)

6. Measurements in deposition plasmas

The HFM was used to investigate different kinds of low pressure plasma deposition processes. First results were obtained for cathodic sputtering in an ICP argon plasma. In this experimental configuration, sputtering of the target is initiated by applying a bias voltage to a metal plate, and is independent from the creation of the RF plasma. This allows to separate the energetic contribution of the sputter-deposition process (SDP) from the sputtering plasma ones (see Figure 14)..

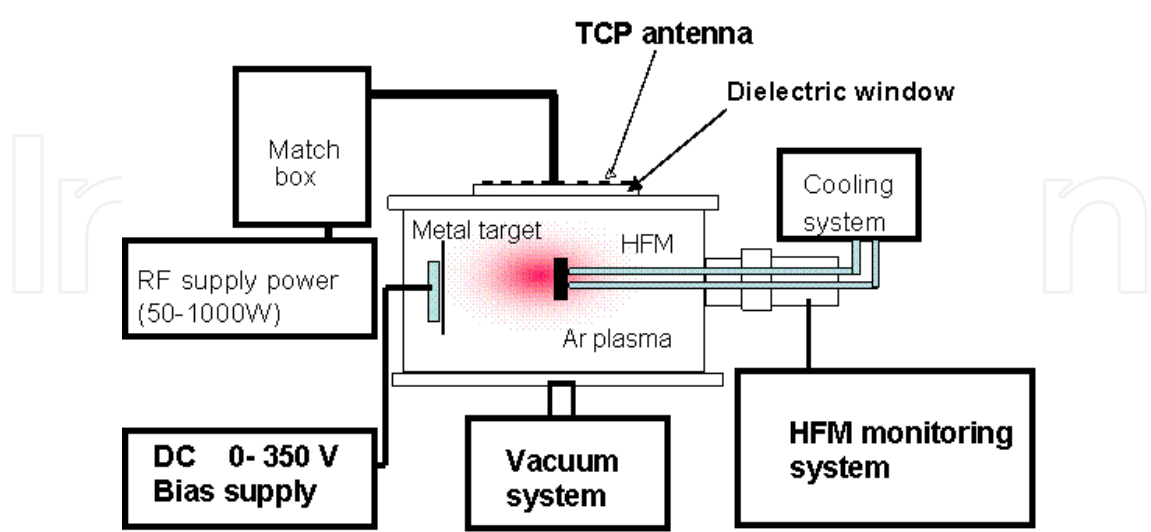


Fig. 14. ICP reactor dedicated to measurements of energy influx in cathodic sputtering deposition process. A plasma is initiated in Ar gas independently from the sputtering process that takes place when the metal target is biased.

Thanks to the good sensitivity of the sensor, the very low contribution of condensing atoms (several  $\text{mW}/\text{cm}^2$ ) was successfully measured. A typical energy flux time evolution recorded during sputtering of iron is presented in Figure 15. This experiment consists of a sequence of six sputter-deposition steps, lasting 1 min each, with  $-200\text{V}$  bias voltage of the target. As soon as the plasma is turned on ( $t \approx 700\text{ s}$ ), the heat flux through the substrate surface increases sharply within 2 s. The plasma contribution (here of about  $250\text{mW}\cdot\text{cm}^{-2}$ ) has been studied in [4] and is due to energy transfer from charged particles, especially Ar ions. After this switching on step, the signal continues to increase until it reaches a steady state (at about  $1600\text{ s}$ ). This behaviour is attributed to the progressive heating of the reactor, inducing radiative transfer from the walls towards the substrate. This thermal contribution is detected by the HFM in addition to the plasma one. It is thus very easy, with the HFM, to separate this low kinetic contribution from the plasma and deposition ones. In Figure 15 (b), signals corresponding to the sputter-deposition steps are clearly evidenced. The evolution of the signal shape has been explained in reference [4]. What should be noted here is that the sputter-deposition energetic contribution (blue arrows) can easily be determined and that the measurement is reproducible.

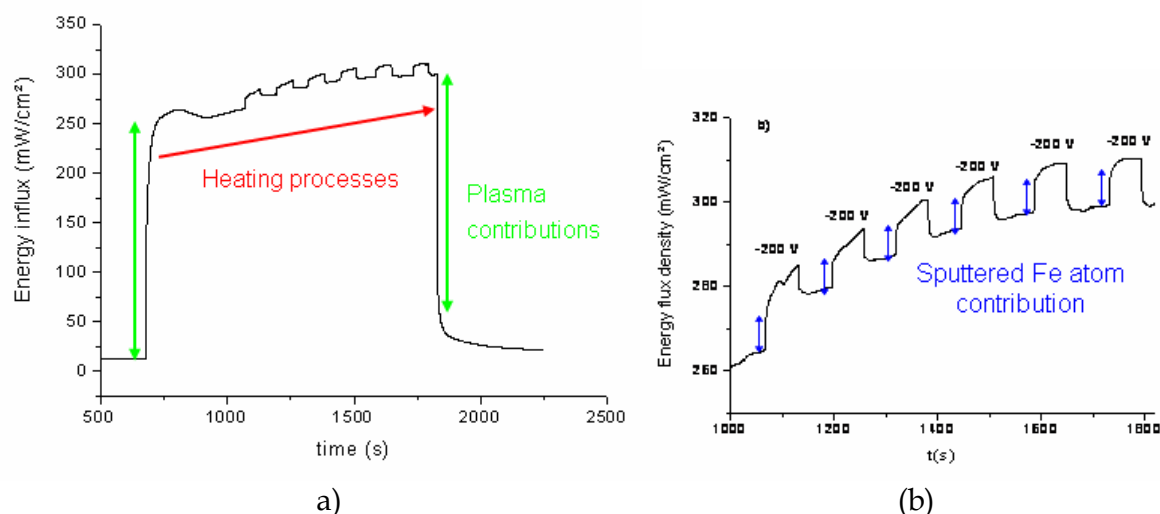


Fig. 15. Fe sputter deposition at  $-200\text{V}$  target bias, in  $0.5\text{ Pa}$  and  $400\text{W}$  argon plasma, (a) Energy flux measurements, (b) zoom of the figure showing the 1 min sputter-deposition. The energetic contributions of Ar plasma and sputtered Fe atoms are clearly distinguished.

From this kind of measurements, the energetic contribution of the sputter-deposition process can be studied and followed versus experimental parameters such gas pressure, accelerating voltage and RF Power. An example is given in Figure 16 in the case of Pt sputtering.

A linear evolution is found for the energy brought by the SDP with respect to the Pt target bias voltage. Obviously, as the target voltage becomes more negative, the kinetic energy of  $\text{Ar}^+$  attracted by the target increases. This leads to a more efficient sputtering process. The metal atoms sputtered out of the target are thus more numerous. It has been shown that, in our experimental configuration, the mean kinetic energy of sputtered atoms only weakly depends on the energy of the incoming argon ions [15, 28, 29]. The increase of the deposition contribution is thus mainly due to a rise in the number of condensing atoms. Another contribution that can participate to the global SPD energy transfer is the one of the argon ions that are reflected by the target, neutralized and form fast neutrals. It can be predicted from simple calculations given for example in [15]. This contribution is also expected to increase with the negative bias voltage. The behaviour observed in figure 15 was thus expected.



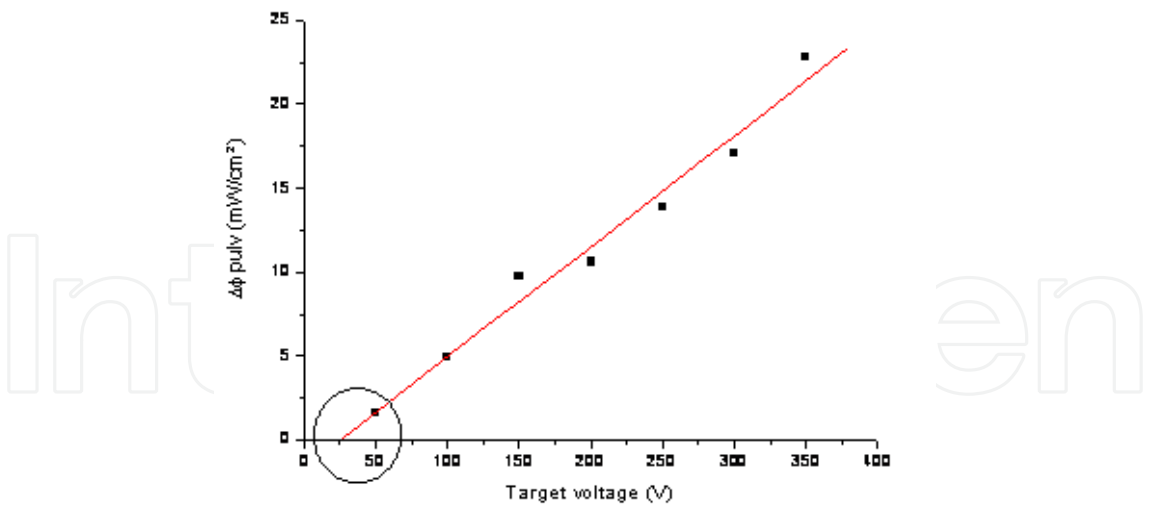


Fig. 16. Energy flux density due to the SPD of Pt versus the target bias voltage in a 0.5 Pa and 400Wargon plasma

In order to study the possible energy brought by fast neutrals, energy balances have been done taking into account the number of Ar ions bombarding the target (calculated from the ionic current), the sputtering and reflection mechanisms [15], and the transport until the substrate. Results are presented in Figure 17 for Pt and Mo.

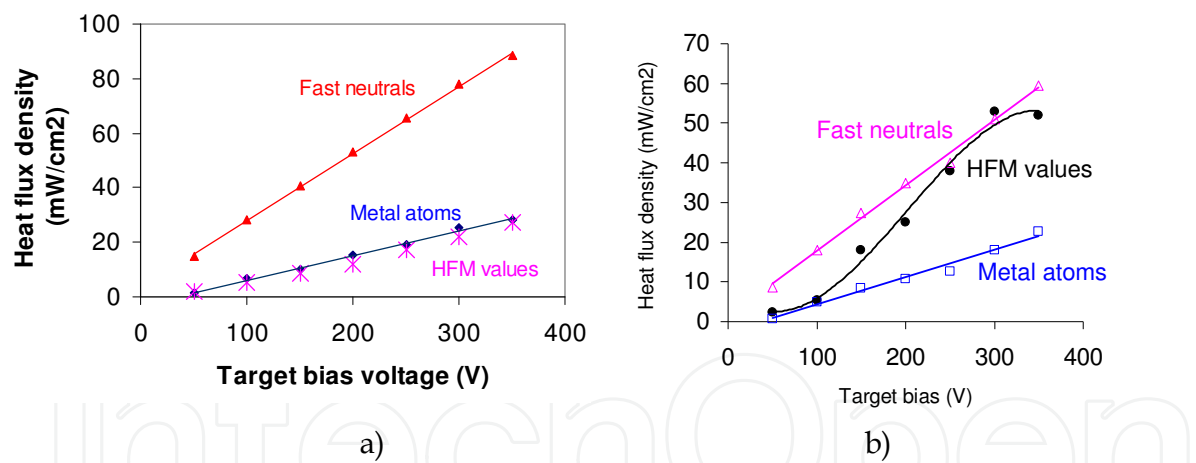


Fig. 17. Evolution of the heat flux density versus the target bias voltage for a) Pt SPD and b) Mo SPD.

The graphs in Fig. 17 clearly show that fast neutrals do not play the same role on the global energy transfer to the substrate depending on the sputtered metal. In the case of Pt, estimated contribution of neutrals is widely higher than the measured heat flux density, showing that the formalism of Drüsedau used in the calculation is not valid in this case. The very good agreement between measurements and calculated metal atom contribution indicates that the only energetic contribution comes from condensing Pt atoms. In the case of Mo, the evolution of HFM values shows that, at low target bias voltages, only metal atoms transfer energy to the substrate, whereas at higher voltages, fast neutrals participate to the global energy flux transfer.

In Figure 16, the target voltage corresponding to  $\varphi_{\text{sput}} = 0$  is about 25V. Taking into account the plasma potential ( $\approx 10$  V in our experimental conditions), the corresponding energy of the sputtering argon ions can be estimated to be 35 eV. It is interesting to compare this value with the sputtering threshold of Pt by Ar<sup>+</sup> given in the literature (25–30 eV) [30]. The good agreement between both values confirms that the energy transfer from metal sputtered atoms is the main contribution in the SDP of Pt.

By dividing the heat flux density by the estimated metal atom flux at the substrate, it is possible to calculate the energy deposited per atom, which is a parameter known to drive the thin film properties. This parameter is given in Figure 18 versus the target bias voltage.

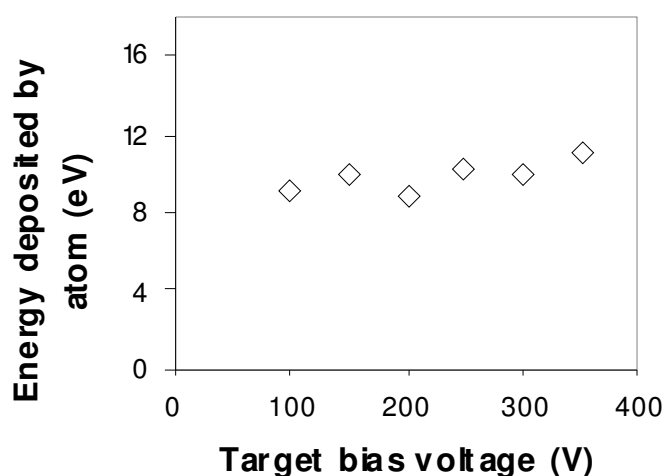


Fig. 18. Evolution of the energy deposited by condensing Pt atoms as a function of the target bias voltage

It is seen from Figure 18 that the energy deposited per atom does not depend on the target bias voltage (in the investigated range). This is in agreement with what is reported in literature [31] and results of our calculations [28]. Indeed, in our ranges of experimental parameters, the kinetic energy of sputtered atoms depends on the gas pressure rather than on the target voltage. The value that can be deduced from the graph is 10.8 eV, which has to be compared to the energy which a Pt atom may release at the substrate surface. Pt atoms carry a kinetic energy estimated to 4.9 eV in the present conditions (0.5 Pa, 10 cm from the target) and transfer their condensation energy, i.e. 5.3 eV, which gives 10.2 eV. The good agreement between calculated and measured values indicates that Pt atoms transfer their whole energy to the surface.

One can wonder if the same energy brought by different species would affect the thin film growth in the same manner. In order to study the role of the energetic vector, deposition of Pt thin films was performed at different locations in the reactor presented in Figure 14. The energetic contributions of both the Ar plasma and the condensing atoms vary. Both contributions are displayed versus the position in the reactor in figure 19. As already reported, in our conditions, the contribution of the plasma is widely higher than the SPD one.

Thin films were deposited at 3 cm and 18 cm from the target. They were analyzed by scanning electron microscopy (SEM) and Rutherford backscattering spectroscopy (RBS). Results are given in figure 20 and Table 4.

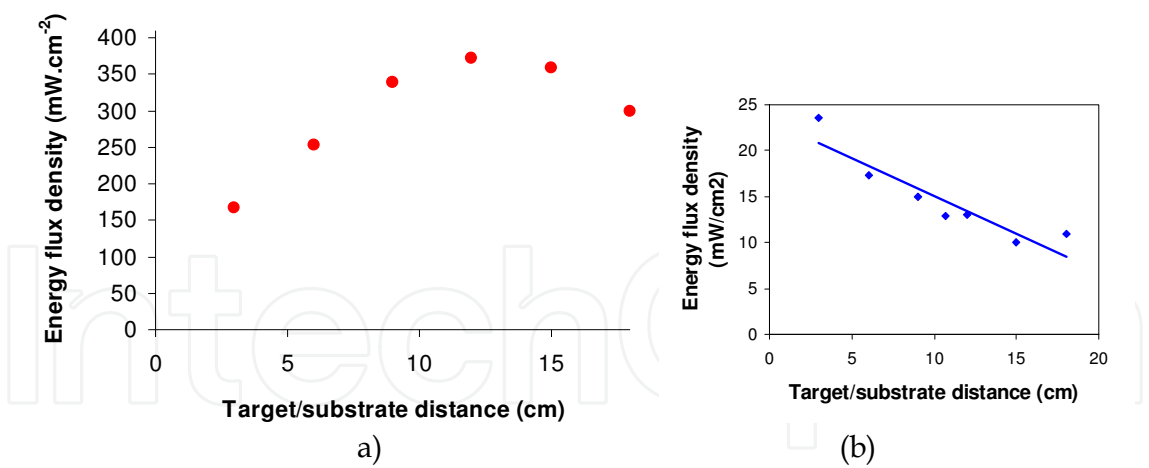


Fig. 19. Evolution of a) plasma and b) SPD energetic contributions versus the distance between the target and the substrate

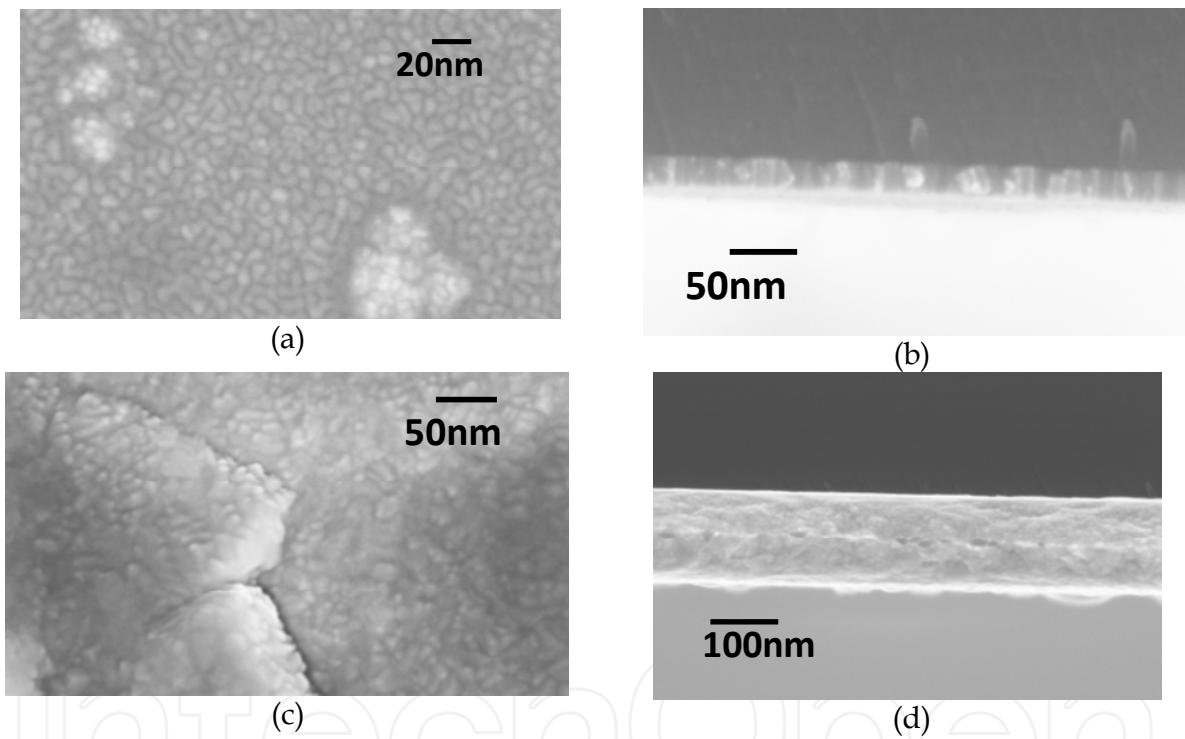


Fig. 20. SEM images of Pt thin films synthesized at 0.5Pa, 400W and -200V target bias voltage ; (a) and (b) target/substrate distance of 18 cm, 30 min deposition time ; (c) and (d) target/substrate distance of 3 cm, 11 min 30 s deposition time.

Echantillon	Pt atom number (RBS) (at/cm2)	Thickness calculated from RBS (nm)	Thickness measured on SEM images (nm)	Deposition rate (at/cm2s)
30min, 18cm	1.1×10 <sup>17</sup>	17	31	6.1×10 <sup>13</sup>
11min30s, 3cm	8.5×10 <sup>17</sup>	128	130	1.2×10 <sup>15</sup>

Table 4. Results from SEM images and RBS. The thickness is determined from RBS results by assuming that the film density is the same as the bulk one. The comparison with the value measured on SEM images gives some insight into the film density.

It is seen from the results above that the Pt film synthesized close to the target (target/substrate distance of 3 cm) is denser and more compact than the one deposited 18 cm away. The energetic deposition conditions deduced from figure 18 are given below:

- distance of 3 cm       $\Delta\phi_{\text{plasma}} = 160 \text{ mW/cm}^2$  and  $\Delta\phi_{\text{dep}} = 24 \text{ mW/cm}^2$

$$\Delta\phi_{\text{global}} = 184 \text{ mW/cm}^2$$

- distance of 18 cm       $\Delta\phi_{\text{plasma}} = 300 \text{ mW/cm}^2$  and  $\Delta\phi_{\text{dep}} = 8 \text{ mW/cm}^2$

$$\Delta\phi_{\text{global}} = 308 \text{ mW/cm}^2$$

It is interesting to note that the global transferred energy is higher far from the target because the Ar plasma contains the most energy at this location. However, the obtained films exhibit low density, which is usually attributed to a growth process that takes place when low energy is available at the surface [20]. Indeed, our results show that the energetic contribution that drives the film characteristics is the energy deposited by the condensing atoms, which is higher at 3 cm. The fact that a minor contribution might play the major role had never been reported until now. This indicates that, as usually done, discussing film properties by only taking account the most abundant species or the one that carries the more energy is not accurate.

## 7. Conclusions

We have shown that the plasma energy flux probe we have developed from a commercial sensor is a relevant and innovative plasma diagnostic. It is able to give direct measurement of the energy influx from the plasma to a surface. The sensor has to be calibrated following a rigorous procedure so that it can be used in low pressure plasmas. We have compared the values given by this sensor to the ones obtained using an other technique developed by colleagues from Kiel [17] and we found a very good agreement between both probes. The main advantages of this sensor rely on the fact that it has a very good time response (17  $\mu\text{s}$  [5]) and that it does not need further data treatment, but gives directly the measured values in real time. This very good time resolution is obtained because of the very thin films, which form the thermopile. The sensitivity of this new sensor was tested in different experiments such as Argon plasma, silicon etching plasma and sputtering deposition plasmas. In all cases, it gave valuable information and measured values were in good agreement with estimations from indirect methods.

This sensor in its commercially available version is well adapted for measurements onto small samples (typically 1  $\text{cm}^2$ ). However, we have shown that it is of particular importance to avoid all kinds of heat flux leaks. If a small thermal bridge is obtained by putting an additional mechanical piece on the sample (for example to fix it), then it will impact the measurement. This is why we decided to just stick the different samples to the sensor directly with a thermal paste.

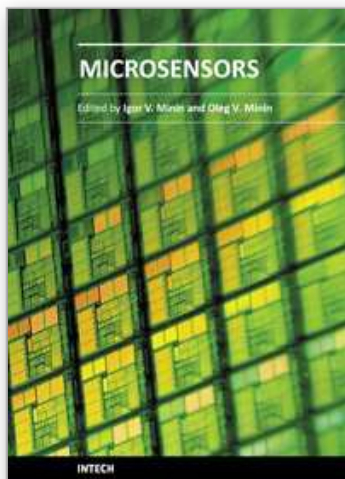
We are now trying to improve the sensor to make it able to measure the energy flux in other conditions. For example, this sensor would be even more of interest for the plasma community if it could be biased. In this case, we would be able to enhance the ion bombardment and evaluate its impact on the energy influx.

This new method in determining the energy influx has opened new research perspectives in the plasma community, especially for materials processing.

## 8. References

- [1] S. Aida and S. Rahmane, *Thin Solid Films* 288, 83 (1996)
- [2] A. Durandet, O. Joubert, J. Pelletier, and M. Pichot, *J. Appl. Phys.* 67, 3862 (1990)
- [3] H. Kersten et Al, *Vacuum* 63, 385 (2001)
- [4] A.L. Thomann et al., *Rev. Scient. Instr.*, 77, 033501 (2006)
- [5] <http://www.vatell.com>
- [6] F. P. Incropera, D. P. DeWitt, *Introduction to Heat Transfer*, 4<sup>th</sup> ed, Wiley, 93-95,(2002).X.
- [7] Zhang , P.Z. Cong and M. Fujii, A Study on Thermal contact resistance at the interface of two solids, *International Journal of Thermophysics*, 27 (3), 880-895, (2006)
- [8] M. J. Persky, Review of black surfaces for space-borne infrared systems, *Review of Scientific Instruments*, 70 (5), 2193-2217 (1999).
- [9] F. M. Devienne, *Advances in Heat Transfer, Low Density Heat Transfer*, 272-352(1965).
- [10] J. A. Thornton *J A 1978 Thin Solid Film* 54 23
- [11] D. J. Ball 1972 *J. Appl. Phys.* 43 3047
- [12] R. Gardon 1953 *The Rev. of Sci. Instrum.* 24 366
- [13] C. Paturaud, G. Farges, M. C. Sainte Catherine and J. Machet 1998 *Surf. Coat. Technol.* 98 1257
- [14] R. Piejak R, V. Godyak, B. Alexandrovich and N. Tishchenko 1998 *Plasma Sources Sci. Technol.* 7 590
- [15] Drüsedau T P, Bock T, John T-M, Klabunde F and Eckstein W 1999 *J. Vac. Sci. Technol. A* 17(5) 2896
- [16] Drüsedau T P, Löhmann M, Klabunde F and John T-M 2000 *Surf. Coat. Technol.* 133–134 126
- [17] Kersten H, Wiese R, Hannemann M, Kapitov A, Scholze F, Neumann H and Hippler R 2005 *Surf. Coat. Technol.* 200 809
- [18] Ellmer K and Mientus R 1999 *Surf. Coat. Technol.* 116–119 1102
- [19] Thornton J A and Lamb J L 1984 *Thin Solid Films* 119 87
- [20] Kersten H, Rohde D, Steffen H, Hippler R, Swinkels G H P M and KroesenGMW2001 *Appl. Phys. A* 72 531
- [21] Wolter M, Stahl M and Kersten H 2009 *Vacuum* 83 768
- [22] Cormier P-A et al 2010 *J. Phys. D : Appl.Phys.* 43 465201
- [23] Lundin D, Stahl M, Kersten H and Helmersson U 2009 *J. Phys. D: Appl. Phys.* 42 185202
- [24] M. A. Lieberman and A. J. Lichtenberg, « *Principles of Plasma Discharges and Materials* » Processing Wiley, New York (1994)
- [25] Ch.Cardinaud, M.C.Peignon, G.Turban, “Si and W etching mechanistic study based on in-situ surface temperature measurements” , *International Symposium on Plasma Chemistry* 11, Loughborough, UK, August 22-27, 1993, Edited by J. Harry
- [26] R. Dussart, A. L. Thomann, L. E. Pichon, L. Bedra, N. Semmar, P. Lefaucheux, J. Mathias, and Y. Tessier, “Direct measurements of the energy flux due to chemical reactions at the surface of a silicon sample interacting with a SF<sub>6</sub> plasma” *Applied Physics Letters* 93, 131502 (2008)
- [27] Bedra L, Thomann A L, Semmar N, Dussart R and Mathias J 2010 *J. Phys. D: Appl. Phys.* 43 065202
- [28] Brault P et al 2000 *Recent Res. Dev. Vac. Sci. Technol.* 2 35
- [29] Wendt R, Ellmer K and Wiesemann 1997 *J. Appl. Phys.* 82 2115
- [30] Yamamura Y, Tawara H 1995 *NIFS-Data Ser.* 23 1
- [31] J. A. Thornton, *Thin Solid Films* 54, 23 (1978).





## **Microsensors**

Edited by Prof. Igor Minin

ISBN 978-953-307-170-1

Hard cover, 294 pages

**Publisher** InTech

**Published online** 09, June, 2011

**Published in print edition** June, 2011

This book is planned to publish with an objective to provide a state-of-art reference book in the area of microsensors for engineers, scientists, applied physicists and post-graduate students. Also the aim of the book is the continuous and timely dissemination of new and innovative research and developments in microsensors. This reference book is a collection of 13 chapters characterized in 4 parts: magnetic sensors, chemical, optical microsensors and applications. This book provides an overview of resonant magnetic field microsensors based on MEMS, optical microsensors, the main design and fabrication problems of miniature sensors of physical, chemical and biochemical microsensors, chemical microsensors with ordered nanostructures, surface-enhanced Raman scattering microsensors based on hybrid nanoparticles, etc. Several interesting applications area are also discusses in the book like MEMS gyroscopes for consumer and industrial applications, microsensors for non invasive imaging in experimental biology, a heat flux microsensor for direct measurements in plasma surface interactions and so on.

### **How to reference**

In order to correctly reference this scholarly work, feel free to copy and paste the following:

Dussart Rémi, Thomann Anne-Lise and Semmar Nadjib (2011). A Heat Flux Microsensor for Direct Measurements in Plasma Surface Interactions, Microsensors, Prof. Igor Minin (Ed.), ISBN: 978-953-307-170-1, InTech, Available from: <http://www.intechopen.com/books/microsensors/a-heat-flux-microsensor-for-direct-measurements-in-plasma-surface-interactions>

**INTech**  
open science | open minds

### **InTech Europe**

University Campus STeP Ri  
Slavka Krautzeka 83/A  
51000 Rijeka, Croatia  
Phone: +385 (51) 770 447  
Fax: +385 (51) 686 166  
[www.intechopen.com](http://www.intechopen.com)

### **InTech China**

Unit 405, Office Block, Hotel Equatorial Shanghai  
No.65, Yan An Road (West), Shanghai, 200040, China  
中国上海市延安西路65号上海国际贵都大饭店办公楼405单元  
Phone: +86-21-62489820  
Fax: +86-21-62489821

© 2011 The Author(s). Licensee IntechOpen. This chapter is distributed under the terms of the [Creative Commons Attribution-NonCommercial-ShareAlike-3.0 License](https://creativecommons.org/licenses/by-nc-sa/3.0/), which permits use, distribution and reproduction for non-commercial purposes, provided the original is properly cited and derivative works building on this content are distributed under the same license.

IntechOpen

IntechOpen